SCIENCE CHINA
Chemistry

•COMMUNICATIONS•

June 2021 Vol.64 No.6: 953–958
https://doi.org/10.1007/s11426-021-9967-9

Atmospheric CO_2 capture and photofixation to near-unity CO by Ti^{3+}-V_o-Ti^{3+} sites confined in TiO_2 ultrathin layers

Liang Liang[1†], Peiquan Ling[1†], Yuhuan Li[1†], Li Li[1], Jiandang Liu[1], Qiquan Luo[2*], Hongjun Zhang[1*], Qian Xu[1], Yang Pan[1], Junfa Zhu[1], Bangjiao Ye[1] & Yongfu Sun[1*]

[1]*Hefei National Laboratory for Physical Science at Microscale, National Synchrotron Radiation Laboratory, University of Science and Technology of China, Hefei 230026, China;*
[2]*Institute of Physical Science and Information Technology, Anhui University, Hefei 230601, China*

Received January 15, 2021; accepted February 23, 2021; published online May 18, 2021

To realize efficient atmospheric CO_2 chemisorption and activation, abundant Ti^{3+} sites and oxygen vacancies in TiO_2 ultrathin layers were designed. Positron annihilation lifetime spectroscopy and theoretical calculations first unveil each oxygen vacancy is associated with the formation of two Ti^{3+} sites, giving a Ti^{3+}-V_o-Ti^{3+} configuration. The Ti^{3+}-V_o-Ti^{3+} sites could bond with CO_2 molecules to form a stable configuration, which converted the endoergic chemisorption step to an exoergic process, verified by *in-situ* Fourier-transform infrared spectra and theoretical calculations. Also, the adjacent Ti^{3+} sites not only favor CO_2 activation into COOH* *via* forming a stable Ti^{3+}–C–O–Ti^{3+} configuration, but also facilitate the rate-limiting COOH* scission to CO* by reducing the energy barrier from 0.75 to 0.45 eV. Thus, the Ti^{3+}-V_o-TiO_2 ultrathinlayers could directly capture and photofix atmospheric CO_2 into near-unity CO, with the corresponding CO_2-to-CO conversion ratio of ca. 20.2%.

TiO_2 ultrathin layers, CO_2 activation, CO_2 photofixation, positron annihilation lifetime spectroscopy

Citation: Liang L, Ling P, Li Y, Li L, Liu J, Luo Q, Zhang H, Xu Q, Pan Y, Zhu J, Ye B, Sun Y. Atmospheric CO_2 capture and photofixation to near-unity CO by Ti^{3+}-V_o-Ti^{3+} sites confined in TiO_2 ultrathin layers. *Sci China Chem*, 2021, 64: 953–958, https://doi.org/10.1007/s11426-021-9967-9

Recently, as monitored by the CO_2-tracking satellites, atmospheric concentrations of CO_2 reach an all-time high of 33 gigatonnes in 2019, which inevitably causes environmental deterioration and climate change [1]. Through mimicking the natural photosynthesis of plants, artificial photocatalysts have been widely fabricated for capturing and converting CO_2 into fuels and value-added products [2]. Although the artificial photosynthetic process may contribute to lower the levels of CO_2 in atmosphere, most of the previous studies require high purity (typically ≥99.99%) of CO_2, which is costly and arduous to be separated and concentrated from ambient air levels (~400 ppm) as well as compressed to typically 11–14 MPa for transportation and storage [3]. In other words, only very limited success has been achieved in low concentration of CO_2 photoreduction, especially under atmospheric-like conditions (~0.04%) [4]. This can primarily be ascribed to thermodynamic stability and kinetic inertness of CO_2 molecule, since the dissociation energy of its C=O bond is as high as ~750 kJ mol^{-1}. More importantly, many of the reported photocatalysts still suffer from low selectivity for the desirable products [5], mainly because of the various possible CO_2 reduction pathways toward different products. To overcome these limitations, major considerations should be prioritised to efficiently capture CO_2 molecules and selectively convert them into the single product.

With regard to the initial CO_2 adsorption process, increasing the number of low-coordinated sites on the surface of catalysts could promote the ability of CO_2 chemisorption, since the surface sites with many dangling bonds can

†These authors contributed equally to this work.
*Corresponding authors (email: yfsun@ustc.edu.cn; hjzhang8@ustc.edu.cn; qluo@ahu.edu.cn)

strongly bind with the CO_2 molecules [6]. Concerning the following CO_2 activation procedure, creating abundant electron-donating sites is able to transform the linear and chemically inert CO_2 molecule to a bent structure, benefiting from the electron donation to the electron-poor carbon atoms [7]. Considering that the product selectivity is closely related to the intermediate configurations on the surface of catalysts [8], it is highly necessary to modulate the binding nature of key reaction intermediates and hence provide the possibility to tailor product selectivity. Taken together, designing a photocatalyst featuring atomic-level thickness and abundant surface defects is highly desirable, where the atomic thickness can maximize the number of surface sites for CO_2 adsorption, while the defect-induced electron localization centers could act as active sites for activating inert CO_2 molecules.

Herein, taking the most widely used photocatalyst of TiO_2 as an example, defective anatase TiO_2 ultrathin layers were first successfully synthesized using the mixed-phase TiO_2 ultrathin layers with a scale of ~1.50 g/batch as the precursor (Figure S1, Supporting Information online). X-ray diffraction (XRD) pattern of the products in Figure 1(a) could be readily indexed to anatase TiO_2, corresponding to JCPDS No. 21-1272. All the peaks in the micro-Raman spectrum (Figure S2) could further verify that the TiO_2 products were in pure anatase phase, where no peaks of any other phases or carbon impurities in the range of 100–1700 cm^{-1} were detected. Moreover, transmission electron microscopy (TEM) image in Figure 1(b) exhibited their freestanding and sheet-like morphology with a lateral size of ca. 200 nm. High-resolution TEM image in Figure S3(a) depicted that the interplanar distances of 2.38 and 3.52 Å corresponded to the (004) and (101) lattice plane distances of the anatase TiO_2. Meanwhile, their dihedral angle of 69° was also fairly consistent with the calculated angle between (004) and (101) planes, implying the [010] orientation of the synthesized TiO_2 ultrathin layers. Atomic force microscopy (AFM) and the corresponding height profiles in Figure S3(b, c) clearly manifested that the average thickness of the as-obtained ultrathin layers was ca. 1.42 nm, which agreed well with the thickness of 7-atom thick TiO_2 slab along the [010] direction. More importantly, as revealed by the X-ray photoelectron spectra (XPS) in Figure 1(c), the Ti 2p spectra could be deconvoluted into two doublets corresponding to the Ti^{4+} ($2p_{3/2}$=458.8 eV) and Ti^{3+} ($2p_{3/2}$=457.4 eV), whereas the O 1s core-level spectra could be fitted by three peaks corresponding to $O_{lattice}$ (530.1 eV), $O_{Ti^{3+}}$ (531.1 eV) and oxygen vacancy (531.4 eV), indicating the formation of Ti^{3+} and oxygen vacancies in the synthesized TiO_2 ultrathin layers [9]. By comparison, the pristine TiO_2 ultrathin layers were also

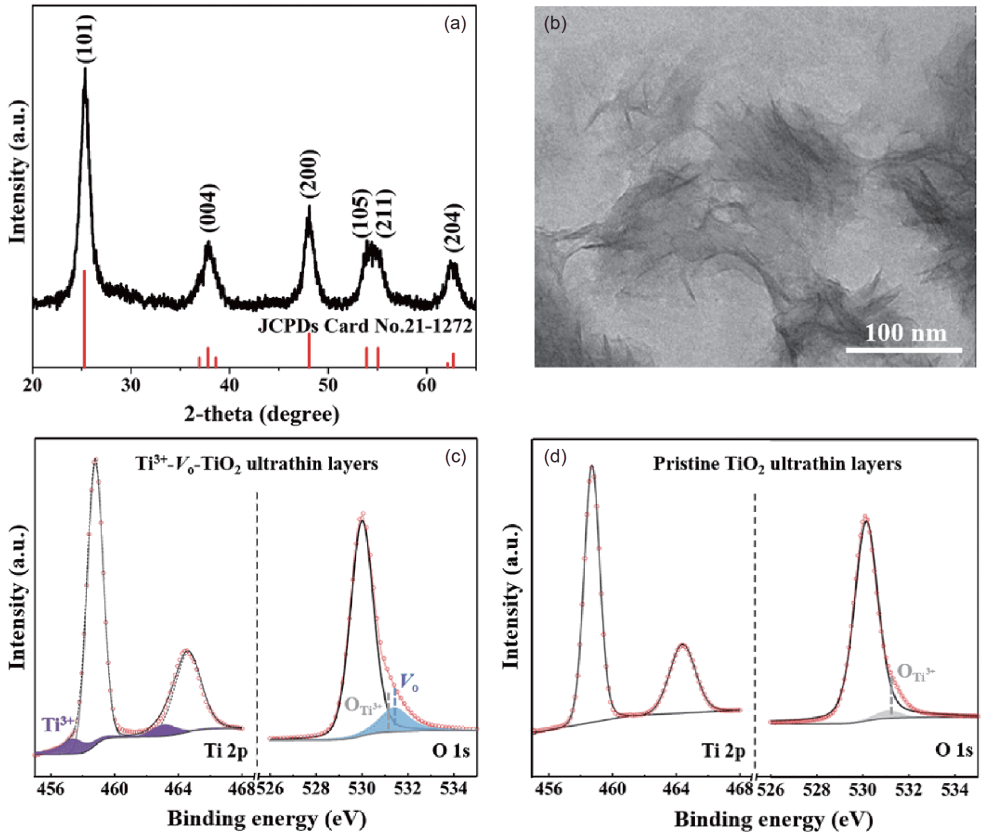

Figure 1 (a) XRD pattern, (b) TEM image for the Ti^{3+}-V_o-TiO_2 ultrathin layers; (c) Ti 2p and O 1s XPS spectra for the Ti^{3+}-V_o-TiO_2 ultrathin layers; (d) Ti 2p and O 1s XPS spectra for the pristine TiO_2 ultrathin layers (color online).

fabricated by tuning the annealing atmosphere (Figure S4), in which no obvious signals for Ti^{3+} and oxygen vacancies were detected by the corresponding XPS spectra in Figure 1 (d), confirming the negligible amount of defect structure within the pristine TiO_2 ultrathin layers.

To further identify the Ti^{3+} and oxygen vacancies in the synthesized defective TiO_2 ultrathin layers, density functional theory (DFT) calculations and positron annihilation lifetime (PAL) spectroscopy were adopted [10,11]. Initially, DFT calculations in Figure S5 illustrated that the bridging oxygen vacancy was easier to be formed within the defective TiO_2 layer slab as compared to other types of oxygen vacancies. In addition, Bader charges of the two nearest-neighbor Ti atoms adjacent to the bridging oxygen vacancy presented 1.79 and 1.75 electrons (Figure 2(a, b)), respectively, which implied their +3 oxidation state by comparing with that of the Ti^{3+} (1.79e) in Ti_2O_3 [12]. Furthermore, as illustrated by the PAL spectra in Figure 2(c, d), Figure S6 and Table 1, the defective TiO_2 ultrathin layers and the pristine TiO_2 ultrathin layers showed three lifetime components. As compared to the calculated positron lifetime values (186.8 ps for defect-free, 192.4 ps for Ti^{3+}-V_o-Ti^{3+}, 195.4 ps for $V_{o\text{-}o}$, 197.5 ps for V_{Ti}, 209.5 ps for $V_{Ti\text{-}O}$, 203.1 ps for $V_{Ti\text{-}Ti}$) and Figure S7, the experimental shortest positron lifetime (τ_1) for both the samples corresponded to positron annihilation at the Ti^{3+}-V_o-Ti^{3+} configuration sites and defect-free region, respectively [11]. The other two longer components (τ_2 and τ_3) for both the samples could be attributed to the large defect clusters and the interface present in the samples, respectively [13]. As an outcome, all the above theoretical and experimental results undoubtedly demonstrated the formation of Ti^{3+}-V_o-Ti^{3+} defective structure in the synthetic TiO_2 ultrathin layers (Ti^{3+}-V_o-TiO_2 ultrathin layers).

To disclose the effects of Ti^{3+}-V_o-Ti^{3+} defective structure on the electronic band structure, synchrotron-radiation photoelectron spectra (SRPES) and ultraviolet-visible spectroscopy (UV-Vis) diffuse reflectance spectra were conducted on the Ti^{3+}-V_o-TiO_2 ultrathin layers and the pristine TiO_2 ultrathin layers [14]. As shown in Figure S8(a), the Ti^{3+}-V_o-TiO_2 ultrathin layers and the pristine TiO_2 ultrathin layers exhibited the band gaps of 3.30 and 3.35 eV, respectively. As clarified by SRPES spectra in Figure S8(b), the Ti^{3+}-V_o-TiO_2 ultrathin layers and the pristine TiO_2 ultrathin layers possessed the work function of 4.20 and 4.25 eV, the valence band maximums of 2.97 and 3.1 V *vs.* normal hydrogen electrode (NHE), and the conduction band minimums of −0.33 and −0.25 V *vs.* NHE, respectively. Based on the above results, the band structures for the Ti^{3+}-V_o-TiO_2 ultrathin layers and the pristine TiO_2 ultrathin layers theoretically matched with the CO_2 reduction and H_2O oxidation potentials simultaneously (Table S1, Supporting Information online), providing the prerequisite to participate in the following reactions.

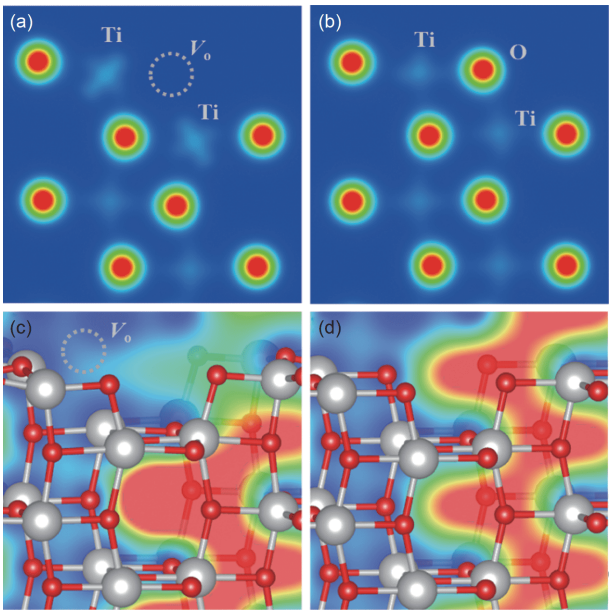

Figure 2 Distribution of charge density for (a) the Ti^{3+}-V_o-TiO_2 ultrathin layer slab and (b) the pristine TiO_2 ultrathin layer slab, plotted from 0 (blue) to 0.035 e $Bohr^{-3}$ (red). Distribution of positron density for (c) the Ti^{3+}-V_o-TiO_2 ultrathin layer slab and (d) the pristine TiO_2 ultrathin layer slab. Bader charges for the Ti sites adjacent to the oxygen vacancy of Ti^{3+}-V_o-TiO_2 ultrathin layer slab are 1.79e and 1.75e, respectively, showing a +3 oxidation state. The grey and red balls in (c, d) represent the Ti and O atoms, respectively (color online).

As is well-known, the rising atmospheric levels of CO_2 raise concerns about the ensuing effects on the global climate. In this respect, conversion of atmospheric CO_2 to hydrocarbons could be expected as a promising way to reduce CO_2 emissions and gain value-added products simultaneously [15]. Considering the unique defective structure and well-matched band structure for TiO_2 ultrathin layers, their CO_2 photoreduction experiments were carried out in the fresh air, simulated air and pure CO_2, respectively. Expectedly, in the fresh air, the Ti^{3+}-V_o-TiO_2 ultrathin layers possessed a CO evolution rate of 23.1 μmol g^{-1} h^{-1} (Figure 3 (a)), which was roughly 2.8 times higher than that of the pristine TiO_2 ultrathin layers; meanwhile, only negligible amount of H_2 was detected and no any other gas or liquid carbonous product was detected by gas chromatography or

Table 1 Analysis results of experimental PAL spectra for the Ti^{3+}-V_o-TiO_2 ultrathin layers and the pristine TiO_2 ultrathin layers, respectively

	τ_1 (ps)	τ_2 (ps)	τ_3 (ns)	I_1 (%)	I_2 (%)	I_3 (%)
Ti^{3+}-V_o-TiO_2 ultrathin layers	192.4±2.2	350.7±0.3	2.150±0.030	10.8±0.2	86.1±0.2	3.1±0.1
Pristine TiO_2 ultrathin layers	188.7±2.9	399.2±0.4	1.616±0.016	6.9±0.1	90.0±0.1	3.1±0.1

^{1}H nuclear magnetic resonance (NMR) during the photocatalysis in the fresh air, thus giving a CO selectivity of near 100%. More importantly, the Ti^{3+}-V_o-TiO_2 ultrathin layers showed the CO_2-to-CO conversion ratio of ca. 20.2% after 9 h photocatalysis in the fresh air (Figure 3(b)), which was obviously higher than the 0.01% conversion ratio in pure CO_2, giving possibilities of the direct implementation of CO_2 in the fresh air. $^{13}CO_2$ isotope-labelling experiments combined with the synchrotron-radiation vacuum ultraviolet photoionization mass spectrometry (SVUV-PIMS) (Figure 3 (c)) further identified the product of ^{13}CO was indeed originated from the reduction of isotope-labeled $^{13}CO_2$. *In-situ* thermographic photographs in Figure S9 depicted that the Ti^{3+}-V_o-TiO_2 ultrathin layers could maintain the temperature at ~26 °C during a catalytic cycle, which demonstrated they could achieve CO_2 photoreduction at room temperature in the fresh air [16]. Furthermore, the Ti^{3+}-V_o-TiO_2 ultrathin layers did not show any obvious attenuation in CO_2 photoreduction activities in the fresh air even after the forth cycle of repetition test up to 36 h, while the post-catalysis characterizations showed their superior photostability (Figure 3 (d) and Figure S10). It is worth noting that these results tested in the fresh air were consistent with that in the simulated air (21.96% O_2 + 78% N_2 + 0.04% CO_2), further verifying the Ti^{3+}-V_o-TiO_2 ultrathin layers could capture atmospheric CO_2 and convert it into valuable products. With regard to the other half reaction, the O_2 evolution rate was measured to be ca. 10.1 μmol g^{-1} h^{-1} after subtraction of the experimental background concentration of O_2 in the air for the Ti^{3+}-V_o-TiO_2 ultrathin layers, which was consistent with the expected stoichiometric ratio (2:1) of CO/O_2 ratio for CO_2 reduction. Taken together, the above results verified that the Ti^{3+}-V_o-TiO_2 ultrathin layers could achieve 20.2% CO_2-to-CO conversion and ~100% CO selectivity in atmospheric CO_2 photoreduction, hence providing a feasible pathway for practical solar fuel applications.

To better understand why the Ti^{3+}-V_o-Ti^{3+} defective sites contributed to improved conversion and selectivity for atmospheric CO_2 reduction, the capture and activation ability of CO_2 for the Ti^{3+}-V_o-TiO_2 ultrathin layers was compared with that of the pristine TiO_2 ultrathin layers. Initially, as displayed by the CO_2 adsorption isotherms in Figure S11, the Ti^{3+}-V_o-TiO_2 ultrathin layers revealed an increased CO_2 adsorption capacity as compared to the pristine TiO_2 ultrathin layers, indicating the stronger adsorption ability on the former sample. To further study the CO_2 adsorption configuration on the surface of Ti^{3+}-V_o-TiO_2 ultrathin layers, *in-situ* Fourier transformed infrared spectroscopy (FTIR) was collected under gas flow of the simulated air and at the presence of water. The peak at 1507 cm^{-1} in Figure 4(a) and Figure S12(a) revealed the presence of monodentate carbonate species, while the peak centered at 1672 cm^{-1} could be assigned to the bidentated carbonate species, confirming the carbonate species of CO_2 adsorption configuration on the

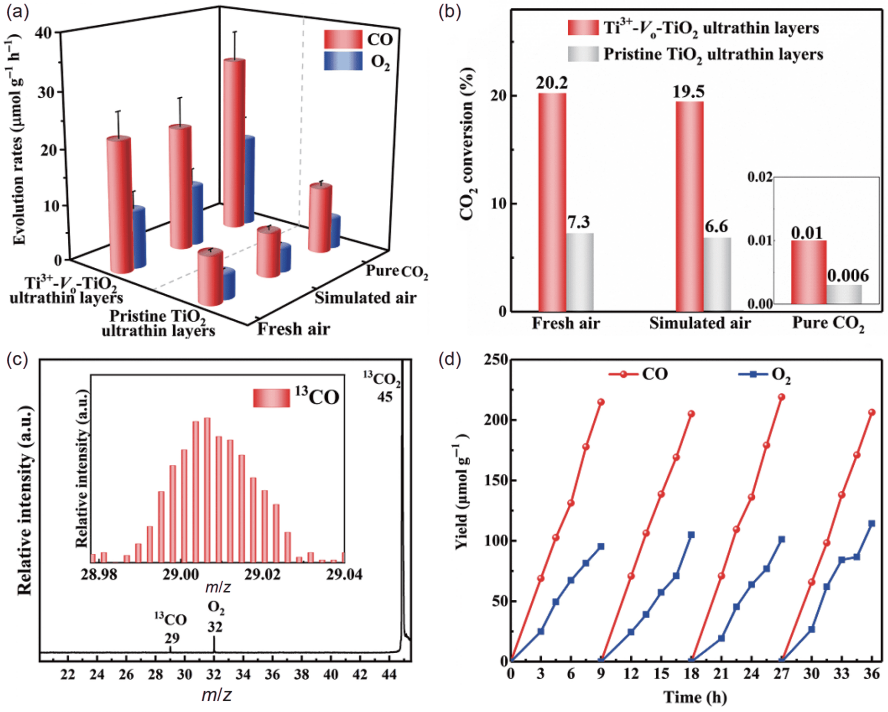

Figure 3 (a) CO_2 photoreduction experiments carried out in the fresh air, simulated air and pure CO_2, respectively, and (b) the corresponding CO_2-to-CO conversion ratio over the Ti^{3+}-V_o-TiO_2 ultrathin layers and the pristine TiO_2 ultrathin layers. (c) SVUV-PIMS spectrum of the products for the Ti^{3+}-V_o-TiO_2 ultrathin layers after $^{13}CO_2$ photoreduction at $h\upsilon$=14.50 eV. Inset gives the corresponding signal of m/z=29 (^{13}CO). (d) Cycling curves of CO and O_2 evolution rates over the Ti^{3+}-V_o-TiO_2 ultrathin layers. The error bars in (a) represent the standard deviations of three independent measurements of the same sample (color online).

surface [17]. To gain insights into the geometric effect and electronic effect of CO_2 adsorption over the Ti^{3+}-V_o-TiO_2 ultrathin layers, the DFT simulations and charge density difference were adopted. As shown in Figure S13, the angle of Ti–O–Ti in the same row as the V_o sites increased from 99.98° to 101.50°, indicating that the geometric effect of V_o sites led to surface relaxation. Once CO_2 is adsorbed, the structure was counteracted with the decrease angle of Ti–O–Ti of 101.12° by achieving a bent CO_2 configuration. Notably, there was charge accumulation in the bonding region between CO_2 and the Ti^{3+}-V_o-Ti^{3+} defective sites (Figure S14), which suggested the strong interaction between CO_2 molecules and the defective sites resulted in originally linear CO_2 molecule's bent configuration with an O–C–O angle (θ in Figure S14) of 135.91° and two elongated C–O bonds of 1.24 and 1.27 Å, respectively, thus forming a relative stable configuration (Figure S15). In addition, the adsorption energy was estimated to be −0.10 eV, further indicating the strong bonding between CO_2 and the Ti^{3+}-V_o-Ti^{3+} defective sites. As comparison, CO_2 adsorption energy on the pristine TiO_2 ultrathin layer slab was calculated to be slightly endothermic with an adsorption energy of +0.02 eV, indicating the pristine surface was relatively difficult to bond with CO_2 due to their intrinsic chemical inertness. The above-mentioned results showed that the exposed Ti^{3+}-V_o-Ti^{3+} defective sites with the presence of excess electrons helped to strengthen the bonding between CO_2 and Ti^{3+}-V_o-Ti^{3+} sites, and thus achieved improved CO_2 adsorption ability. Moreover, the Ti^{3+}-V_o-TiO_2 ultrathin layers exhibited the decreased intensity of the photoluminescence emission spectra (Figure S16) and increased surface photovoltage (SPV) response intensity (Figure S17) relative to the pristine TiO_2 ultrathin layers, suggesting the Ti^{3+}-V_o-Ti^{3+} defective sites were beneficial for photogenerated electron-hole separation, and hence able to afford more electrons to activate CO_2 molecules [18].

To further investigate the CO_2 activation process, *in-situ* FTIR spectra were performed to probe the reaction intermediates over the Ti^{3+}-V_o-TiO_2 ultrathin layers. As shown in Figure 4(b) and Figure S12(b), a distinct peak appeared at ca. 1622 cm^{-1} could be assigned to hydrocarboxyl ($COOH^*$) intermediate, suggesting the CO_2 could be reduced into CO *via* the $COOH^*$ intermediates [19]. Based on the above experimental results, the DFT calculations (Figure 4(c), Figure

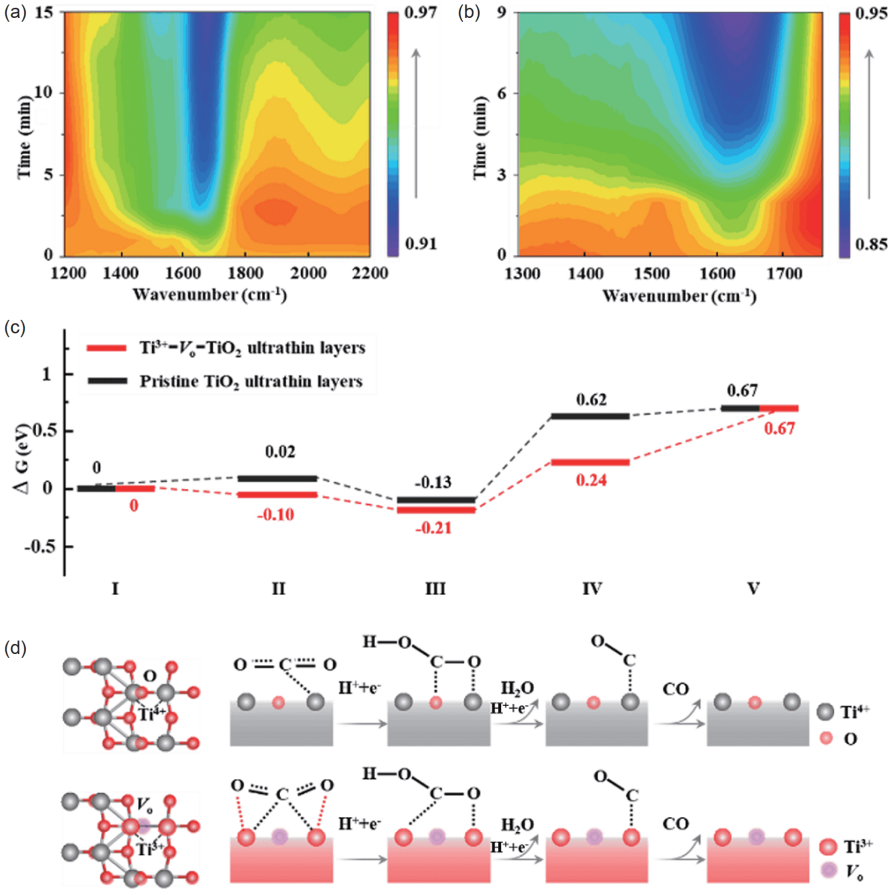

Figure 4 (a) 2D contour map of *in-situ* FTIR spectra for the CO_2 adsorption over the Ti^{3+}-V_o-TiO_2 ultrathin layers; (b) 2D contour map of *in-situ* FTIR spectra for the reaction intermediates during the CO_2 photoreduction process over the Ti^{3+}-V_o-TiO_2 ultrathin layers; (c) free energy diagrams of CO_2 photoreduction and (d) schemes for the corresponding key elementary steps (*I*-*V*) over the Ti^{3+}-V_o-TiO_2 ultrathin layer slab and the pristine TiO_2 ultrathin layer slab, respectively (color online).

S18 and Table S2) were performed to simulate the process of CO_2 reduction. In the step of the protonation of the adsorbed CO_2 to form an adsorbed COOH* intermediate (Figure 4(d)), two Ti^{3+} sites in the Ti^{3+}-V_o-Ti^{3+} defective sites could bond with COOH* to form a bridge configuration of Ti^{3+}–C–O–Ti^{3+}, resulting in a lowered energy barrier for COOH* formation. Note that the subsequent step of COOH* scission to CO* was regarded as the rate-limiting step, which showed an energy barrier of 0.45 eV, obviously lower than the 0.75 eV for the pristine TiO_2 ultrathin layer slab. Besides, the Ti^{3+} sites on the Ti^{3+}-V_o-TiO_2 ultrathin layer slab helped to stabilize the CO* intermediate with a stronger CO binding energy of −0.43 eV as compared to that of the pristine TiO_2 layer slab (−0.05 eV), suggesting that the formation of Ti^{3+}-CO provided an additional driving force for the scission step of COOH* to CO*. Accordingly, the Ti^{3+}-V_o-Ti^{3+} defective sites in the TiO_2 ultrathin layers not only facilitated CO_2 capture from air, but also benefited for the CO_2 activation process and the following rate-limiting COOH* scission step, which definitely promoted CO_2 photoreduction performance in the fresh air.

In summary, for directly capturing and effectively activating atmospheric CO_2 molecules, abundant Ti^{3+}-V_o-Ti^{3+} defective sites confined in TiO_2 ultrathin layers were designed and fabricated. XPS spectra demonstrated the presence of Ti^{3+} and V_o in the synthetic TiO_2 ultrathin layers, while Bader charge calculations and PAL spectra first disclosed the formed oxygen vacancies were associated with the formation of two adjacent Ti^{3+} sites. *In-situ* FTIR spectra and DFT calculations unveiled these generated Ti^{3+}-V_o-Ti^{3+} sites could simultaneously bond with the C and O atoms of CO_2 molecules to form a stable bridge adsorption configuration, which converted the endoergic chemisorption step to an exoergic process, showing feasibility for capturing CO_2 directly from the air. More importantly, the two adjacent Ti^{3+} sites not only facilitated CO_2 activation into COOH* through forming a stable Ti^{3+}–C–O–Ti^{3+} configuration, but also lowered the rate-limiting energy barrier from 0.75 to 0.45 eV *via* stabilizing the produced CO*. As a result, the Ti^{3+}-V_o-TiO_2 ultrathin layers could directly capture CO_2 in the fresh air and selectively photofix the atmospheric CO_2 into near-unity CO, in which the CO_2-to-CO conversion ratio was ca. 20.2%, giving possibilities of the direct implementation of CO_2 in the fresh air. Thus, this defect design concept for tailoring atmospheric CO_2 capture and activation opens up broad possibilities for "real-world" application of solar fuel production.

Acknowledgements This work was supported by the National Key R&D Program of China (2019YFA0210004, 2017YFA0207301, 2017YFA0303500), the National Natural Science Foundation of China (21975242, U2032212, 21890754, 21805267, 21703222, 11975225), the Strategic Priority Research Program of Chinese Academy of Sciences (XDB36000000), Youth Innovation Promotion Association of CAS (CX2340007003), Key Research Program of Frontier Sciences of CAS (QYZDY-SSW-SLH011), Major Program of Development Foundation of Hefei Center for Physical Science and Technology (2020HSC-CIP003), Users with Excellence Program of Hefei Science Center CAS (2020HSC-UE001), The University Synergy Innovation Program of Anhui Province (GXXT-2020-001), and the Fok Ying-Tong Education Foundation (161012). Supercomputing USTC and National Supercomputing Center in Shenzhen are acknowledged for computational support.

Conflict of interest The authors declare no conflict of interest.

Supporting information The supporting information is available online at http://chem.scichina.com and http://link.springer.com/journal/11426. The supporting materials are published as submitted, without typesetting or editing. The responsibility for scientific accuracy and content remains entirely with the authors.

1 Tong D, Zhang Q, Zheng Y, Caldeira K, Shearer C, Hong C, Qin Y, Davis SJ. *Nature*, 2019, 572: 373–377
2 (a) Bard AJ, Fox MA. *Acc Chem Res*, 1995, 28: 141–145; (b) Lv H, Sa R, Li P, Yuan D, Wang X, Wang R. *Sci China Chem*, 2020, 63: 1289–1294; (c) He Q, Wu B, Hu Y, Huang W, Li Y. *Sci China Chem*, 2020, 63: 1716–1720
3 House KZ, Baclig AC, Ranjan M, van Nierop EA, Wilcox J, Herzog HJ. *Proc Natl Acad Sci USA*, 2011, 108: 20428–20433
4 (a) Gao P, Li S, Bu X, Dang S, Liu Z, Wang H, Zhong L, Qiu M, Yang C, Cai J, Wei W, Sun Y. *Nat Chem*, 2017, 9: 1019–1024; (b) Han B, Ou X, Deng Z, Song Y, Tian C, Deng H, Xu YJ, Lin Z. *Angew Chem Int Ed*, 2018, 57: 16811–16815; (c) Wu X, Li Y, Zhang G, Chen H, Li J, Wang K, Pan Y, Zhao Y, Sun Y, Xie Y. *J Am Chem Soc*, 2019, 141: 5267–5274
5 Matavos-Aramyan S, Soukhakian S, Jazebizadeh MH, Moussavi M, Hojjati MR. *Appl Mater Today*, 2020, 18: 100499
6 Cao N, Chen Z, Zang K, Xu J, Zhong J, Luo J, Xu X, Zheng G. *Nat Commun*, 2019, 10: 2877
7 (a) Huygh S, Bogaerts A, Neyts EC. *J Phys Chem C*, 2016, 120: 21659–21669; (b) Dong H, Zhang L, Li L, Deng W, Hu C, Zhao ZJ, Gong J. *Small*, 2019, 15: 1900289
8 Li X, Sun Y, Xu J, Shao Y, Wu J, Xu X, Pan Y, Ju H, Zhu J, Xie Y. *Nat Energy*, 2019, 4: 690–699
9 (a) Wang Y, Sun H, Tan S, Feng H, Cheng Z, Zhao J, Zhao A, Wang B, Luo Y, Yang J, Hou JG. *Nat Commun*, 2013, 4: 2214; (b) Kumar PM, Badrinarayanan S, Sastry M. *Thin Solid Films*, 2000, 358: 122–130
10 Ji Y, Luo Y. *J Am Chem Soc*, 2016, 138: 15896–15902
11 Kansy J. *Nucl Instrum Meth A*, 1996, 374: 235–244
12 Liu R, Fang L, Hao Y, Chi Y. *Materials*, 2018, 11: 2156
13 Kong M, Li Y, Chen X, Tian T, Fang P, Zheng F, Zhao X. *J Am Chem Soc*, 2011, 133: 16414–16417
14 Jiao X, Zheng K, Liang L, Li X, Sun Y, Xie Y. *Chem Soc Rev*, 2020, 49: 6592–6604
15 Nakajima T, Tamaki Y, Ueno K, Kato E, Nishikawa T, Ohkubo K, Yamazaki Y, Morimoto T, Ishitani O. *J Am Chem Soc*, 2016, 138: 13818–13821
16 Liang L, Li X, Sun Y, Tan Y, Jiao X, Ju H, Qi Z, Zhu J, Xie Y. *Joule*, 2018, 2: 1004–1016
17 Tumuluri U, Howe JD, Mounfield Iii WP, Li M, Chi M, Hood ZD, Walton KS, Sholl DS, Dai S, Wu Z. *ACS Sustain Chem Eng*, 2017, 5: 9295–9306
18 Han Q, Bai X, Man Z, He H, Li L, Hu J, Alsaedi A, Hayat T, Yu Z, Zhang W, Wang J, Zhou Y, Zou Z. *J Am Chem Soc*, 2019, 141: 4209–4213
19 Mino L, Spoto G, Ferrari AM. *J Phys Chem C*, 2014, 118: 25016–25026